Inorganic Chemistry

pubs.acs.org/IC

Article

Pressure-Driven Structural and Electronic Transitions in a Two-Dimensional Janus WSSe Crystal

Meiling Hong, Lidong Dai,* Haiying Hu,* Xinyu Zhang, Chuang Li, and Yu He

Cite This: *Inorg. Chem.* 2023, 62, 16782−16793

Read Online

ACCESS | Metrics & More | Article Recommendations | Supporting Information

ABSTRACT: In this work, we presented the first report on the high-pressure structural stability and electrical transport characteristics in WSSe under different hydrostatic environments through Raman spectroscopy, electrical conductivity, and high-resolution transmission electron microscopy (HRTEM) coupled with first-principles theoretical calculations. For nonhydrostatic conditions, WSSe endured a phase transition at 15.2 GPa, followed by a semiconductor-to-metal crossover at 25.3 GPa. Furthermore, the bandgap closure was accounted for the metallization of WSSe as derived from theoretical calculations. Under hydrostatic conditions, ∼ 2.0 GPa pressure hysteresis was detected for the emergence of phase transition and metallization in WSSe because of the feeble deviatoric stress. Upon depressurization, the reversibility of the phase transition was substantiated by those of microscopic HRTEM observations under different hydrostatic environments. Our high-pressure investigation on WSSe advances the insightful understanding of the crystalline structure and electronic properties for the Janus transition-metal dichalcogenide (TMD) family and boosts prospective developments in functional devices.

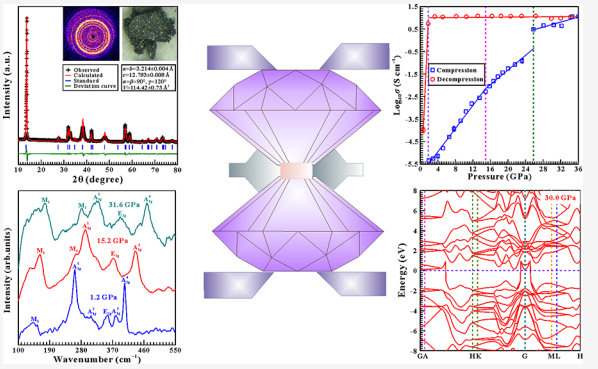

1. INTRODUCTION

Recently, TMDs come into focus due to their exceptional mechanical, optical, and electronic properties and prospective applications in nanoelectronics, optoelectronics, spintronics, and valleytronics.[1−3] As a new branch of the TMD family, Janus TMDs with the general formula of MXY (M = Mo, W; X ≠ Y = S, Se, and Te) are constituted by the stacking of the asymmetric X−M−Y atomic layers alongside the *c* direction via van der Waals interactions.[4] Unlike the mirror-symmetric TMDs, the out-of-plane asymmetry in Janus TMDs leads to the distinctive properties of intrinsic electrical dipole, strong Rashba spin−orbit coupling (SOC), large valley splitting, strong piezoelectric effect, and excellent catalytic performance, endowing them with immense prospects in electromechanical and optoelectrical devices, sensors, and photocatalysts.[5−9] As a prototypical member of Janus TMD family, tungsten sulfoselenide (WSSe) crystallizes in the hexagonal symmetry with a finite bandgap of 1.42 eV under ambient conditions.[10,11]

The crystalline structure and electrical configuration of TMDs can be effectively manipulated by the internal and external stimuli, such as temperature, pressure, light, electric field, magnetic field, and so forth.[1,12−27] Among these approaches, high pressure has been proven as a clean and maneuverable manner, giving rise to plenteous novel physical phenomena, including the pressure-induced structural transition, amorphization, metallization, and superconductivity.[1,15−29] Despite the fact that tremendous efforts have been devoted to individual molybdenum-based and tungsten-based TMDs, only one available high-pressure investigation on the structural stability and electrical transport behaviors for ternary Janus TMD has been reported to date.[1,15−21,23−25,27] Bera et al. studied the high-pressure structural, vibrational, and electronic properties of MoSSe up to 30.0 GPa using a diamond anvil cell (DAC) by means of synchrotron X-ray diffraction, Raman spectroscopy, and first-principles theoretical calculations.[27] The authors revealed that MoSSe experienced a low-pressure phase transition at ∼3.0 GPa, followed by an isostructural phase transition (IPT) from the $2H_c'$ phase to the mixture of the $2H_c'$ and $2H_a'$ phases at ∼10.8 GPa triggered by the layer sliding. As the pressure was increased to ∼18.0 GPa, MoSSe transformed into the metallic $2H_a'$ phase. Since the pressure-driven IPT and semiconductor-to-metal electronic crossover that emerged in molybdenum dichalcogenides (MoS_2 and $MoSe_2$) resemble those in tungsten dichalcogenides (WS_2 and WSe_2), it is often expected that their correspondent Janus TMDs possess the analogous structural and electrical transport characteristics under high pressure.[1,15−21,23−25,27] Inspired by recent high-pressure research on MoSSe, it remains unclear

Received: June 27, 2023
Published: September 29, 2023

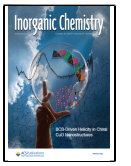

https://doi.org/10.1021/acs.inorgchem.3c02144
Inorg. Chem. 2023, 62, 16782−16793

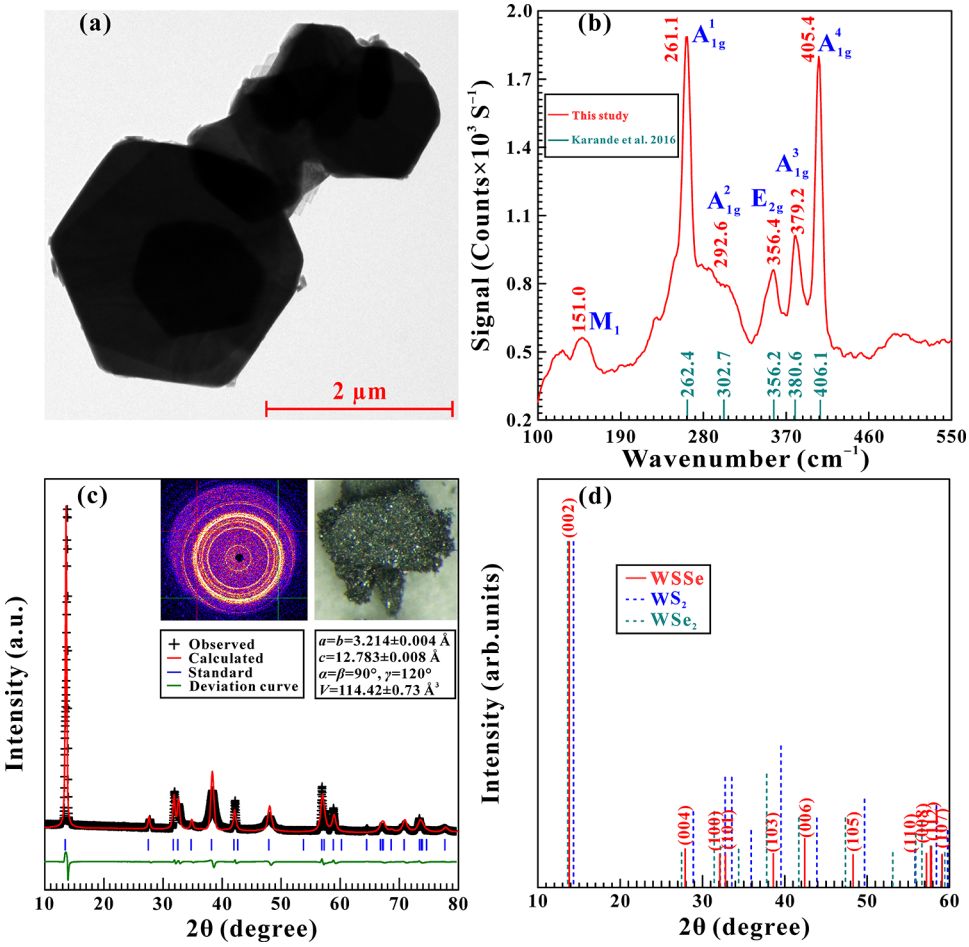

Figure 1. (a) Low-magnification TEM image of the starting specimen; (b) Raman spectrum of the initial sample and comparison with earlier work. The vertical bars present the characteristic Raman peak positions of WSSe reported by Karande et al. (c) Micro-X-ray diffraction spectrum along with the structural refinement for WSSe under atmospheric conditions. The red solid line and black crosses represent the Rietveld fits for the calculated and observed results, respectively. Vertical blue ticks correspond to the standardized peak positions. The deviation curve of the measurement is depicted as the green solid line. Inset: optical photograph, two-dimensional diffraction rings, and corresponding lattice parameters for Janus WSSe. (d) XRD pattern of WSSe together with that of hexagonal WS_2 and WSe_2 for comparison.

whether similar structural and electronic transitions will occur in the same periodic tungsten-based Janus TMD of WSSe.[27]

On the other hand, the degree of hydrostaticity within the sample chamber of DAC is of great significance in influencing the structural stability, the phase transition pressure, and the reversibility of phase transition for some representative TMDs.[18,21−24,26] Furthermore, the degree of hydrostaticity highly depends on the used pressure media (PM) in high-temperature and high-pressure experiments.[30−32] Among the various PM, inert gases (e.g., helium, neon, argon, nitrogen, etc.) can provide the excellent hydrostatic environment, which has been extensively applied to explore the physicochemical characterizations of TMDs under extreme conditions.[15−18,23,24,26,33] As for WSSe, an important ingredient of Janus TMDs, the relevant investigation of the influence of hydrostaticity on its high-pressure structural behaviors is still deficient.

In the present work, the high-pressure structural, vibrational, and electrical transport properties on WSSe up to 40.0 GPa under different hydrostatic environments were comprehensively investigated via Raman spectroscopy, alternating current impedance spectroscopy, and HRTEM in conjunction with first-principles theoretical calculations. Furthermore, the pressure-tuned phase transition and metallization of WSSe as well as the underlying physical mechanisms were deeply explored in detail.

2. EXPERIMENTAL DETAILS

2.1. Sample Characterization. High-purity (99.999%) WSSe crystals with shiny black luster were purchased from Six-Carbon Technology Company (Shenzhen, China), which was synthesized by the chemical vapor deposition (CVD) method.[34] The morphology, crystalline quality, and crystallographic structure of the pristine specimen were characterized by TEM, Raman spectroscopy, and micro-X-ray diffraction (XRD). From the low-magnification TEM image (see Figure 1a), the starting sample exhibits an almost perfect hexagonal shape. Figure 1b displays the selected Raman spectrum of the initial sample, and further, six intense Raman peaks at 151.0, 261.1, 292.6, 356.4, 379.2, and 405.4 cm^{-1} were discerned over the wavenumber range of 100−550 cm^{-1}, in accordance with prior results.[5,35,36] Afterward, the XRD pattern of pristine specimen was recorded using a SmartLab-type X-ray powder diffractometer, equipped with copper Kα radiation operating at the 40 kV accelerated voltage and 20 mA applied current. The sharp diffraction peaks in Figure 1c implied that the starting sample has good crystallinity. As expected, the XRD pattern of WSSe is analogous to those of WS_2 and WSe_2. In comparison with the standard PDF data of the hexagonal WS_2 and WSe_2, we found that all characteristic diffraction peaks of

https://doi.org/10.1021/acs.inorgchem.3c02144
Inorg. Chem. 2023, 62, 16782−16793

WSSe are located between those of WS_2 and WSe_2, satisfying the Bragg equation with the diffraction peaks shifted toward lower angles as the chalcogen atomic radius increased. Furthermore, the obtained XRD data of the starting sample were processed with the Rietveld refinement utilizing the General Structure Analysis System (GSAS) software package,[37] yielding the correspondent lattice parameters for the pristine sample: $a = b = 3.214 \pm 0.004$ Å, $c = 12.783 \pm 0.008$ Å, $\alpha = \beta = 90°$, $\gamma = 120°$, and $V = 114.42 \pm 0.73$ Å^3 under ambient conditions. It is clear that there exist some inevitably subtle deviations between the observed and calculated results, which is highly correlated with atomic coordinates, the occupancies in the unit cell, and the crystalline orientation of the two-dimensional Janus WSSe crystal.[38,39] Moreover, the detailed crystallographic data for WSSe are illustrated in Table S1 of the Supporting Information. Collectively, our results manifested that the pristine sample belongs to the high-quality Janus WSSe with hexagonal symmetry.

2.2. High-Pressure Raman Scattering Measurements. A piston−cylinder-type DAC possessing a pair of 200 μm-diameter culets was exploited for high-pressure Raman scattering and electrical conductivity measurements of WSSe. A piece of 250 μm-thick T-301 stainless steel was prepressed into 50 μm, and then a hole of 100 μm in diameter was laser-drilled at the center of indentation to be the sample cavity. Thereafter, the experimental sample along with ruby employed to calibrate pressure was sealed into the sample chamber for Raman scattering measurements. Two groups of high-pressure Raman spectroscopy experiments were accomplished, i.e., one adopted helium as the PM to realize the hydrostatic condition, whereas no PM was applied in another run for nonhydrostatic condition. The Raman spectra of WSSe were collected in back-scattering geometry by using a Renishaw InVia Raman microscope coupled to an argon ion (514.5 nm) as the excitation source.

2.3. High-Pressure Electrical Conductivity Measurements. In electrical conductivity experiments, a fine mixture of boron nitride and epoxy was densely pressurized into the preindented T-301 stainless steel of a 180 μm-diameter hole, which can be utilized as the insulating substance and the solid pressure medium affording the nonhydrostatic condition.[17,40] Subsequently, another central hole with a diameter of 100 μm was manufactured and served as the insulating sample chamber. To achieve absolute insulation, the residual section of the gasket was covered by the insulation cement. Two slices of electrodes were configured parallel into the upper and lower counterparts of the sample chamber. The *in situ* alternating current impedance spectra of WSSe were measured with a Solartron-1260 impedance/gain-phase analyzer in sweeping frequency mode over the frequency range of 10^{-1} to 10^7 Hz at a typical signal voltage of 3.0 V. In the variable-temperature electrical conductivity experiments, the sample was first compressed to the desired pressures at room temperature and stepwise cooled to 120 K with liquid nitrogen. The temperature was precisely determined by a K-type thermocouple adhered to the lateral diamond anvil. More experimental details were described elsewhere.[21−24,26,41,42]

2.4. HRTEM Observation. The initial and depressurized specimens under different hydrostatic environments were homogeneously scattered into ethanol by ultrasonication for 20 min, and thereafter, a droplet was deposited onto a holey carbon-coated copper grid for HRTEM observations. The HRTEM images and fast Fourier transformation (FFT) patterns for samples were taken using a JEOL JEM-F200 field emission transmission electron microscope with an accelerated voltage of 200 kV. Furthermore, the interplanar spacings of samples were accurately measured with Digital Micrograph software.

2.5. First-Principles Theoretical Calculations. All theoretical calculations of WSSe were accomplished within the framework of density functional theory (DFT) as implemented in the Vienna *ab initio* simulation package (VASP) at 0−40.0 GPa in the Hefei Advanced Computing Center of China.[43−46] The projector augmented wave (PAW) scheme within the generalized gradient approximation (GGA) was adopted to deeply explore the electron−ion interactions.[47,48] The plane-wave kinetic cutoff energy was set at 800 eV to realize high convergence. All structures of WSSe were sufficiently relaxed until the force on each atom was smaller than 0.01 eV Å^{-1}. Two relatively denser k-meshes of $9 \times 9 \times 3$ and $21 \times 21 \times 7$ were employed to successfully achieve high-quality theoretical calculations of the lattice parameters and electronic band structures, which satisfied the convergent criterion with energy differentiation of less than 1 meV per atom. To fully take into account the influence of van der Waals interactions during the first-principles theoretical calculations, the DFT-D3 correction method was applied to precisely calculate the structural relaxation and electronic structure.[49]

3. RESULTS AND DISCUSSION

3.1. High-Pressure Raman Spectroscopy Results. Figure 2a−c shows the high-pressure Raman spectra of WSSe over the pressure range of 1.2−31.6 GPa in non-hydrostatic conditions. Six characteristic Raman peaks of WSSe at 151.0, 261.1, 292.6, 356.4, 379.2, and 405.4 cm^{-1} were identified at 1.2 GPa. Specifically, four prominent Raman peaks located at 261.1, 292.6, 379.2, and 405.4 cm^{-1} are the out-of-plane (A_{1g}) modes in association with the Se−W, S−W−Se, and S−W vibrations.[34−36] Meanwhile, the Raman peak at 356.4 cm^{-1} corresponds to the in-plane (E_{2g}) mode in connection with the S−W vibration. For clarity, the Raman peaks at 261.1, 292.6, 379.2, and 405.4 cm^{-1} were designated as the A^1_{1g}, A^2_{1g}, A^3_{1g}, and A^4_{1g} modes, respectively. In addition, a feeble Raman peak located at 151.0 cm^{-1} was nominated as the M_1 mode of WSSe, which originates from the superposition of $E_{2g(S-W)}$-$LA_{(S-W)}$ and $A_{1g(Se-W)}$-$LA_{(Se-W)}$ modes.[50]

As seen in Figure 2a−c, all Raman peaks of the sample exhibited monotonous blueshifts with the application of pressure, revealing the enhanced interaction between atoms. At the same time, the M_1 Raman peak became intense and sharp, which coincided with the progressive weakening of the A^3_{1g} Raman peak under pressurization. Note that the A^2_{1g} Raman peak became stronger below 8.4 GPa, whereas it tended to appreciably decay beyond 8.4 GPa. As the pressure approached 15.2 GPa, the A^2_{1g} and A^3_{1g} Raman peaks vanished, unveiling that the out-of-plane vibrations play a paramount role in triggering the phase transition of WSSe. When the pressure was higher than 15.2 GPa, a new peak emerged as the left shoulder of the A^1_{1g} Raman peak, which was labeled as the M_2 Raman peak of WSSe. Moreover, the M_2 Raman peak became stronger by applying pressure. When the pressure exceeded 15.2 GPa, the remaining Raman peaks of the sample monotonically moved toward higher wavenumbers. More specifically, as the pressure was increased, the remarkable broadening of Raman peaks and the substantial decline of Raman intensity in WSSe provided robust evidence for the occurrence of phase transition above 25.3 GPa. Furthermore, the Raman shift and Raman fwhm are important parameters for elucidating the emergence of pressure-driven phase transition in TMDs.[1,15−27] Figures 2d and 3 display the variation of Raman shifts and Raman fwhm's with applied pressure for WSSe, and further, their corresponding linear fitting results are tabulated in Tables S2 and S3 of the Supporting Information, respectively. Particularly, both the Raman shifts for M_1, M_2, A^1_{1g}, and E_{2g} along with A^4_{1g} modes, as well as the Raman fwhm's of A^1_{1g} and A^4_{1g} modes presented discernible inflection points at 15.2 and 25.3 GPa, which further proved the emergence of phase transitions in WSSe. Upon depressurization, the Raman peaks of the sample showed redshifts, concomitant with the gradual enhancement in

https://doi.org/10.1021/acs.inorgchem.3c02144
Inorg. Chem. 2023, 62, 16782−16793

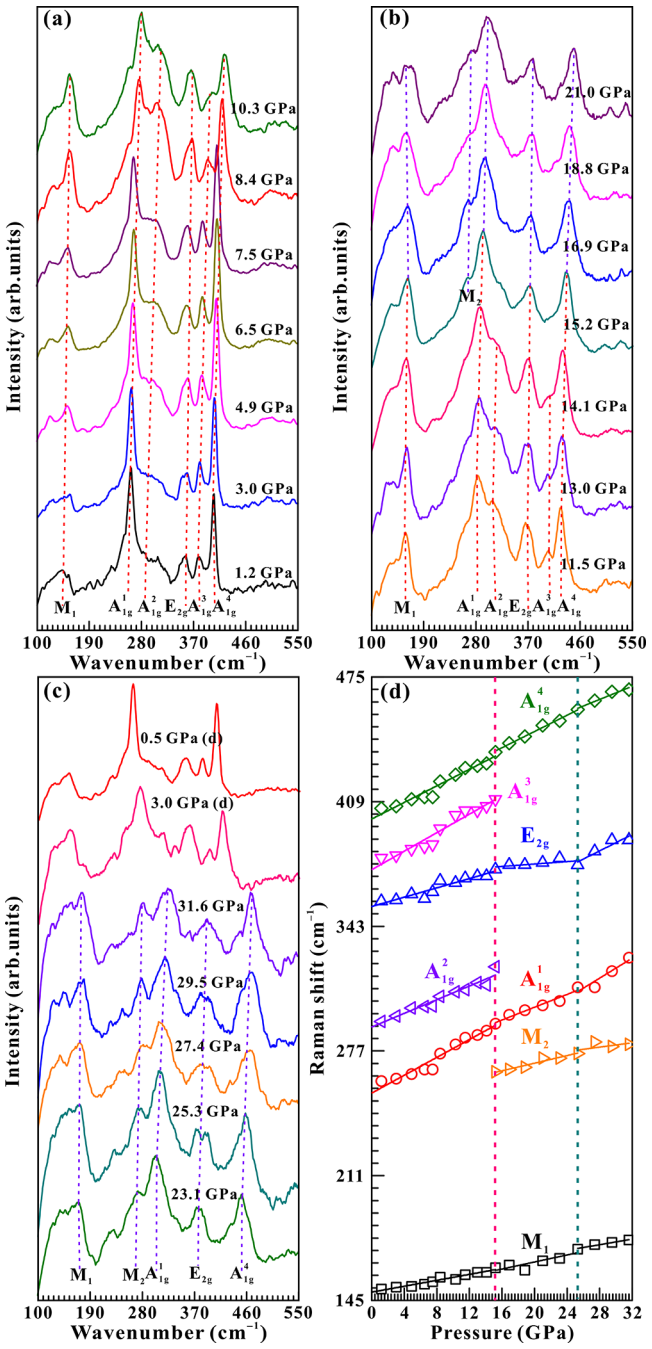

Figure 2. High-pressure Raman scattering results for WSSe at the respective pressure ranges of (a) 1.2−10.3 GPa, (b) 11.5−21.0 GPa, and (c) 23.1−31.6 GPa during pressurization and two typical Raman spectra at 3.0 and 0.5 GPa upon depressurization. (d) Evolution of Raman shift against pressure for WSSe under nonhydrostatic conditions. Herein, d stands for depressurization.

Raman peak intensity. In addition, the Raman peak intensity ratios of A^1_{1g}/A^2_{1g}, E_{2g}/A^2_{1g}, A^4_{1g}/A^2_{1g}, and A^1_{1g}/A^4_{1g} upon pressurization and depressurization in both nonhydrostatic and hydrostatic conditions are presented in Table S4 of the Supporting Information. Under nonhydrostatic conditions, the Raman peak intensity ratios of A^1_{1g}/A^2_{1g}, E_{2g}/A^2_{1g}, A^4_{1g}/A^2_{1g}, and A^1_{1g}/A^4_{1g} upon compressed 1.2 and 3.0 GPa, as well as 0.5 GPa upon depressurization, are nearly identical. However, the Raman peak intensity ratios of A^1_{1g}/A^2_{1g}, E_{2g}/A^2_{1g}, A^4_{1g}/A^2_{1g}, and A^1_{1g}/A^4_{1g} upon decompressed 3.0 GPa are slightly distinct. As the pressure relieved to 3.0 GPa, the high-pressure phase did not completely transform into the original WSSe due to the pronounced pressure hysteresis. Upon further depressurization to 0.5 GPa, both of the Raman peak positions and Raman peak intensity ratios were reverted to the initial values, evidencing the reversibility of phase transition.[51]

Figure 3 and Figure S1 in the Supporting Information show the high-pressure Raman spectroscopic results on WSSe and their relevant relations of Raman shifts and Raman fwhm's versus pressure under hydrostatic pressurization. As a whole, the evolution of Raman profiles, Raman shifts, and Raman fwhm's with pressure for WSSe under hydrostatic conditions was reproducible with those under nonhydrostatic conditions. In the case of hydrostatic pressurization, WSSe underwent a phase transition at 17.5 GPa, followed by another phase transition at 27.3 GPa. Notably, the phase transitions of WSSe were postponed by ∼2.0 GPa under hydrostatic conditions as compared to that under nonhydrostatic conditions, which can be reasonably interpreted by the weak deviatoric stress.[21−24,26] With the rise in pressure, the considerable enhancement of deviatoric stress under nonhydrostatic conditions with respect to that under hydrostatic conditions plays a critical role in facilitating the appearance of structural transitions in WSSe.

3.2. High-Pressure Electrical Conductivity Results.

Figure 4a−c illustrates the Nyquist plots of impedance spectra for WSSe under the conditions of 1.9 and 36.1 GPa and atmospheric temperature. At 1.9−7.7 GPa, each impedance spectrum of sample consists of a semicircular arc over the high-frequency range of ∼10^2 to 10^7 Hz corresponding to the grain interior contribution plus an inclined straight line in the low-frequency region of ∼10^{-1} to 10^2 Hz attributed to the grain boundary contribution. When the pressure elevated to 9.2 GPa, the tilted straight line successively disappeared, and only one semicircular arc was detectable. Further pressurization to 18.8 GPa showed a sloping line in the fourth quadrant. To quantify the resistances (R) of WSSe, a suitable equivalent circuit of R_{gi}−CPE_{gi} (here, the R_{gi} and CPE_{gi} represent the resistance and constant phase element of the grain interior, respectively) was selected to fit the high-frequency impedance semicircular arcs ranging from 1.9 to 17.7 GPa, and the single R was adopted to fit the oblique lines beyond 18.8 GPa using ZView software. Afterward, the electrical conductivity (σ) of WSSe was determined using the following equation:

$$\sigma = L/SR \quad (1)$$

wherein S and L stand for the cross-sectional area of electrodes (cm^2) and the distance between electrodes (cm). Figure 4d presents the logarithmic electrical conductivity against pressure for WSSe during the compressed and decompressed processes. The electrical conductivity of WSSe is 4.94×10^{-6} S cm^{-1} at the lowest measured pressure of 1.9 GPa, which is close to the previously available result with the electrical conductivity of 3.94×10^{-6} S cm^{-1} under ambient conditions and validates the reliability of our electrical conductivity measurements.[52] Between 1.9 and 14.9 GPa, the electrical conductivity of the sample markedly raised by more than 3 orders of magnitude at a large rate of 0.26 S cm^{-1} GPa^{-1}, followed by the gentle enhancement in electrical conductivity at a moderate speed of 0.16 S cm^{-1} GPa^{-1} at 14.9−23.2 GPa. After 25.8 GPa, weak pressure-dependent electrical conductivity at a minor slope of

https://doi.org/10.1021/acs.inorgchem.3c02144
Inorg. Chem. 2023, 62, 16782−16793

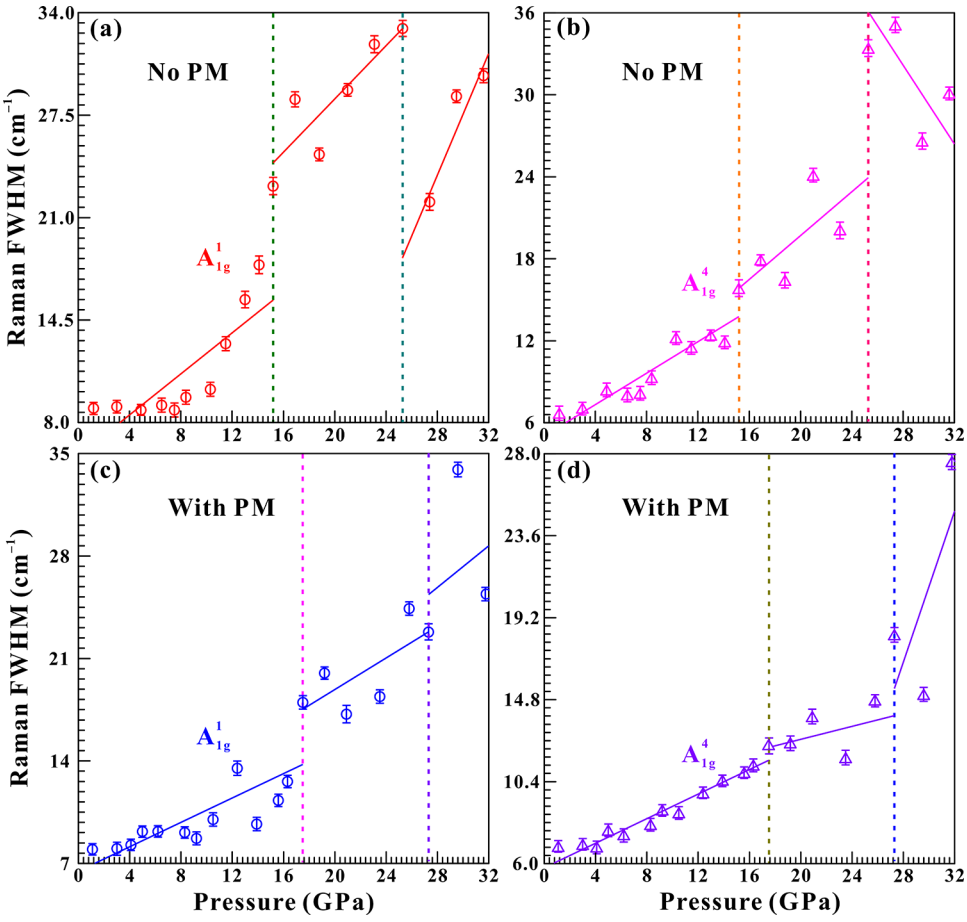

Figure 3. Variation of Raman fwhm against pressure for WSSe under (a, b) nonhydrostatic conditions and (c, d) hydrostatic conditions. Therein, the sign of PM denotes the pressure medium.

0.055 S cm^{-1} GPa^{-1} was detectable. Concurrently, the pressure dependence of CPE within the pressure range of 1.9−17.7 GPa is displayed in Figure 5. Below 14.9 GPa, the CPE elevated marginally with the increase in pressure at a feeble rate of 6.59 × 10^{-12} S cm^{-2} s^{-n} GPa^{-1}. When the pressure was higher than 14.9 GPa, a marked enhancement in the CPE at a relatively large slope of 6.79 × 10^{-10} S cm^{-2} s^{-n} GPa^{-1} was acquired. Consequently, both the electrical conductivity and CPE of the sample exhibited discontinuous changes at 14.9 and 25.8 GPa, which likely correlates with the phase transitions of WSSe. Strikingly, the electrical conductivity of the sample (0.48 S cm^{-1}) at 25.8 GPa reached up to the representative magnitude of metal, signaling the appearance of semiconductor-to-metal crossover.[21−24,26,41,42] Upon depressurization, the electrical conductivity of the sample turned out to be almost invariant ranging from 34.2 to 1.8 GPa. As the pressure released from 1.8 to 0.7 GPa, a conspicuous descent in electrical conductivity by roughly 5 orders of magnitude suggested the reversibility of phase transition, in line with our high-pressure Raman scattering results under different hydrostatic environments.

3.3. Temperature-Dependent Electrical Conductivity Results. To substantiate the presence of metallization in pressurized WSSe, variable-temperature electrical conductivity experiments were implemented upon pressurization and depressurization. Based on solid-state physics theory, the semiconductor exhibits positive temperature dependence of electrical conductivity relation arising from the thermally excited carriers, whereas metal is characterized by the negative temperature dependence of electrical conductivity relation stemming from the enhancement of electron−phonon scattering.[1,15−18,21−24,26,41,42] As plotted in Figures 6a and Figure S2 of the Supporting Information, WSSe exhibits the semiconducting behavior below ∼24.2 GPa, as proven by the upturn of electrical conductivity with the rise in temperature ($d\sigma/dT > 0$). In contrast, the sample presents the metallic feature beyond ∼25.9 GPa with the subtle decline in electrical conductivity as the temperature was raised ($d\sigma/dT < 0$). From Figures 6b and Figure S3 in the Supporting Information, the metal-to-semiconductor conversion takes place at ∼1.4 GPa during depressurization.

Generally speaking, when molybdenum dichalcogenides (MoS_2 and $MoSe_2$) and tungsten dichalcogenides (WS_2 and WSe_2) are subjected to high pressure, the layer sliding IPT and semiconductor-to-metal crossover occurred.[1,18−21,23] We compared the phase transition and metallization pressures of WSSe with those of the same periodic group of TMDs and Janus TMD under different hydrostatic environments in detail, as given in Table S5 of the Supporting Information. For the same mixed chalcogenides, the higher phase transition and metallization pressures of WSSe than those of MoSSe can be explained by the larger atomic radius and broader electron orbitals of tungsten than those of molybdenum, resulting in stronger interlayer interactions. Under the condition of the identical cation, the metallization pressure of WSSe is comparable to that of WSe_2, while it is substantially lower than that of WS_2, as previously reported in MoSSe.[27] The

https://doi.org/10.1021/acs.inorgchem.3c02144
Inorg. Chem. 2023, 62, 16782−16793

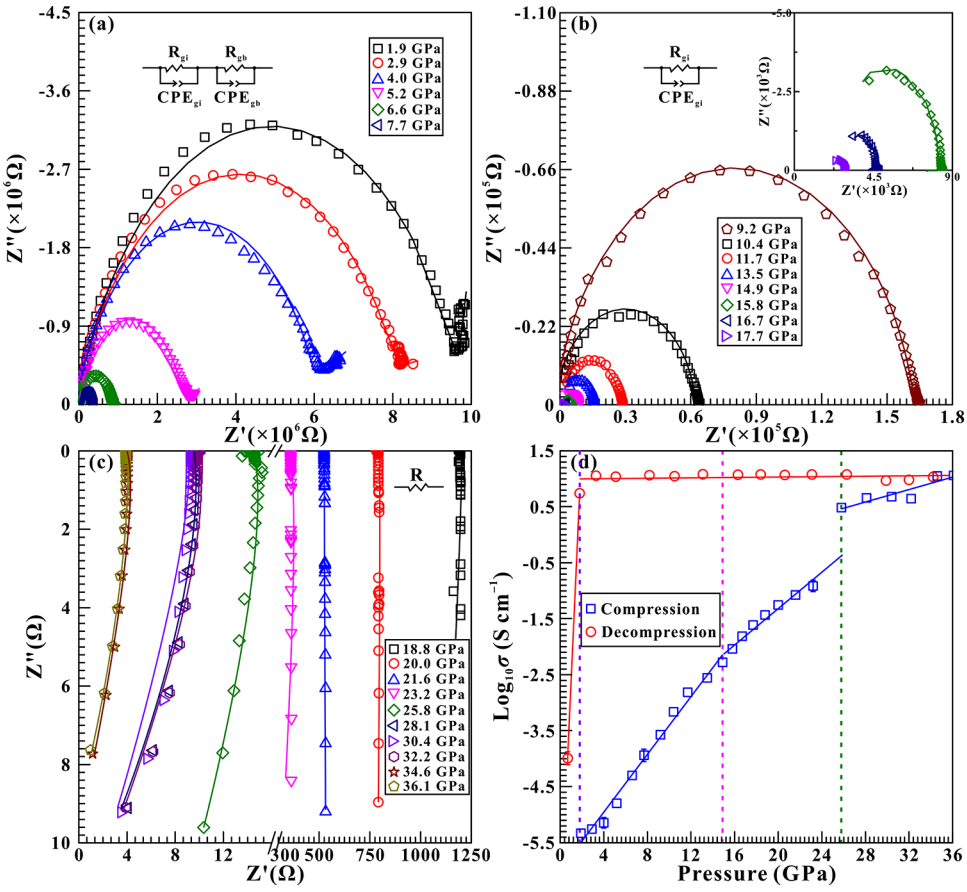

Figure 4. Nyquist diagrams for the impedance spectra in WSSe at the respective pressure ranges of (a) 1.9−7.3 GPa, (b) 9.2−17.7 GPa, and (c) 18.8−36.1 GPa. (d) Pressure-dependent logarithmic electrical conductivity for WSSe upon pressurization and depressurization. Herein, R_{gi} and CPE_{gi} denote the resistance and constant phase element of the grain interior, respectively. The signs of Z' and Z'' represent the real and imaginary parts of complex impedance spectroscopy, respectively. In addition, all of these colored correspondent curves represent the fitting results of the impedance spectra.

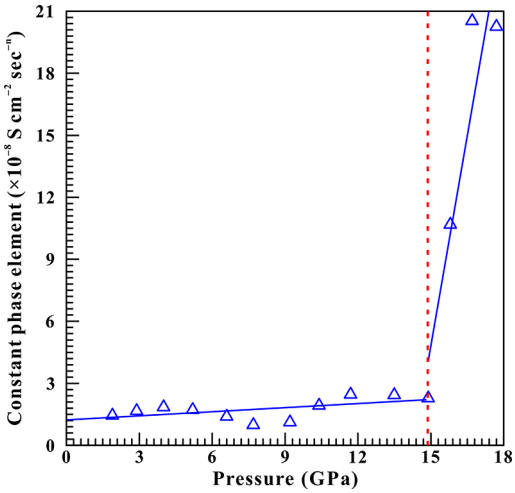

Figure 5. Pressure-dependent constant phase element for WSSe within the pressure range of 1.9−17.7 GPa.

lower electronic transition pressure of WSSe may be attributed to the chemical ordering of sulfur and selenium atoms on the anionic sublattice, which is caused by the moderate lattice mismatch between WS_2 and WSe_2.[27] When both the cation and anion are varied, the metallization pressure of WSSe is close to $MoSe_2$, while it is higher than that of MoS_2. This is presumably stemmed from the broader electron orbitals of tungsten than molybdenum, as well as the more delocalized 4p orbitals of selenium than the 3p orbitals of sulfur, contributing to the enhancement of electronic stability in WSSe.[53] On the other hand, hydrostaticity has been proven to be a critical factor in influencing the high-pressure structural behaviors of TMDs under different hydrostatic environments.[18,21−24,26] Although the hydrostaticity has a feeble influence on the phase stability and reversibility of WSSe, the structural transition and metallization were postponed by ∼2.0 GPa under hydrostatic conditions.

3.4. HRTEM Results. Figure 7 shows the representative HRTEM patterns and their corresponding FFT images for the pristine and decompressed specimens under different hydrostatic environments so as to evaluate the impact of high pressure and PM on the microscopic crystalline structures of WSSe. As portrayed in Figure 7a, the pristine specimen presents homogeneous and vivid lattice fringes, signifying high crystallinity. Afterward, the interplanar spacing for pristine specimen was determined as 0.31 nm, which was ascribed to the (004) crystallographic plane of WSSe. Furthermore, the corresponding FFT pattern suggested that the starting sample is well crystallized in hexagonal symmetry. In light of the HRTEM and FFT images of the initial and recovered samples, the analogous interplanar spacings and the similar diffraction spots hinted the reversibility of structural phase transition in

https://doi.org/10.1021/acs.inorgchem.3c02144
Inorg. Chem. 2023, 62, 16782−16793

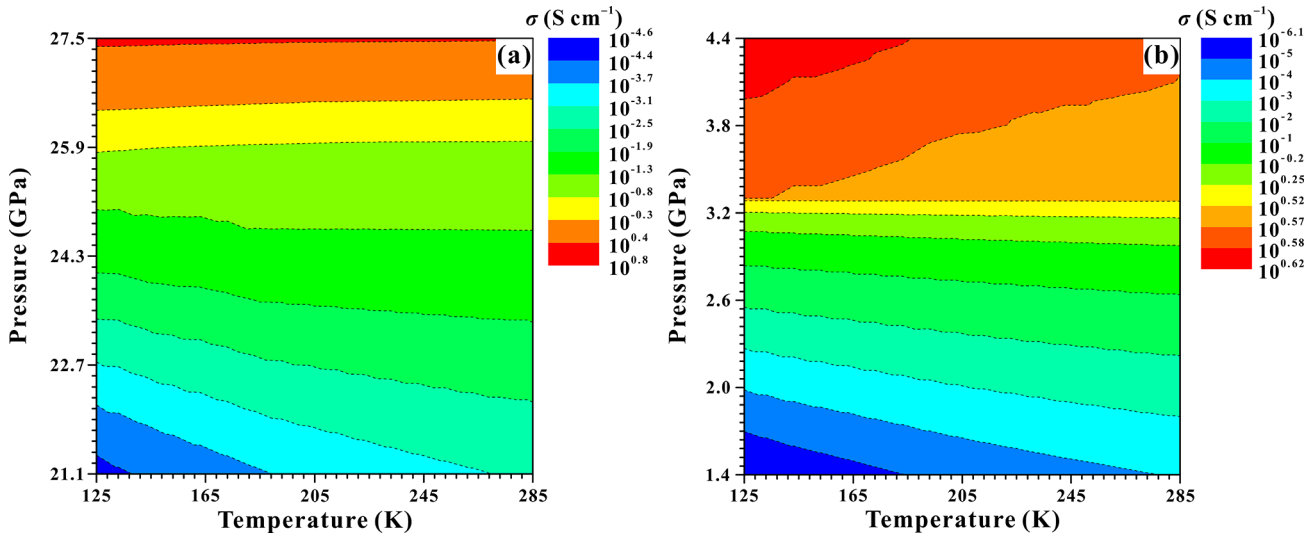

Figure 6. Temperature−pressure−electrical conductivity contour maps for WSSe during (a) pressurization and (b) depressurization.

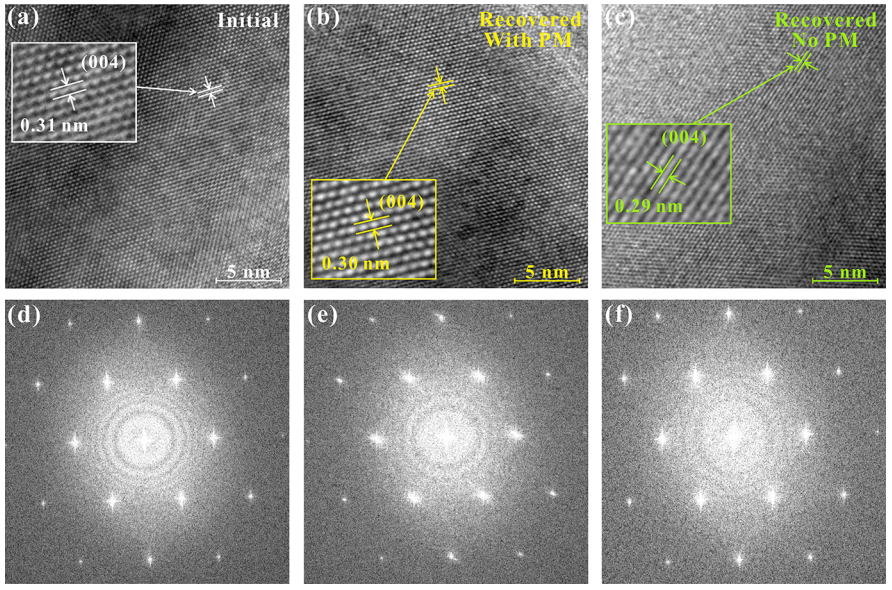

Figure 7. HRTEM patterns and their correspondent FFT images for WSSe. (a, d) Pristine specimen; (b, e) decompressed sample released from 32.1 GPa under hydrostatic conditions; (c, f) depressurized specimen quenched from 31.9 GPa under nonhydrostatic conditions. Here, the sign of PM is the pressure medium.

WSSe under different hydrostatic environments. Nevertheless, the well-resolved lattice fringes and the well-defined diffraction spots for the decompressed sample under hydrostatic conditions relative to those under nonhydrostatic conditions can be reasonably interpreted by the presence of PM, resembling other representative two-dimensional (2D) layered compounds (e.g., $CrCl_3$, $CrBr_3$, HfS_2, etc.).[26,41,54]

3.5. First-Principles Theoretical Calculation Results. For the sake of unveiling the underlying mechanisms on the pressure-driven phase transformation and electronic transition, first-principles theoretical calculations of WSSe were carried out at 0−40.0 GPa. Under ambient conditions, the optimized cell constants of $a = b = 3.27$ Å, $c = 14.72$ Å, and $V = 132.8$ Å^3 with the inequivalent W−S and W−Se bond lengths of 2.43 and 2.55 Å in WSSe conform well to prior studies, justifying the reliability of our theoretical calculations.[6,7,55] Moreover, the lattice parameters of WSSe fall between those of WS_2 and WSe_2.[56] The critical crystalline parameters of the enthalpy, lattice constants (a, b, and c), normalized lattice constants (a/a_0, b/b_0, and c/c_0), lattice constant ratios (a/c and b/c), unit cell volume (V), normalized unit cell volume (V/V_0), bond lengths (W−S, W−Se, and W−W), and bond angles (S−W−S, Se−W−Se, and S−W−Se) under high pressure are illustrated in Figures 8 and Figure S4 of the Supporting Information, respectively. In light of the pressure homology principle, WSSe, the isomorphous intermediate material of WS_2 and WSe_2, is expected to endure an IPT from $2H_c$ to $2H_a$ modifications by applied pressure.[27,57,58] As presented in Figure 8a, the enthalpies of $2H_c$ and $2H_a$ phases of WSSe were calculated within the pressure range of 0−40.0 GPa at a given Hubbard U parameter of 2.9 eV. Apparently, the enthalpy of the $2H_c$ phase is more favorable than the $2H_a$ phase, implying the structural stability of the $2H_c$ phase up to 40.0 GPa. With the increase in pressure, the a and b axes were consecutively contracted, whereas the c axis displayed an observable discontinuity at 14.0 GPa. More precisely, as the pressure was elevated from 0 to

https://doi.org/10.1021/acs.inorgchem.3c02144
Inorg. Chem. 2023, 62, 16782−16793

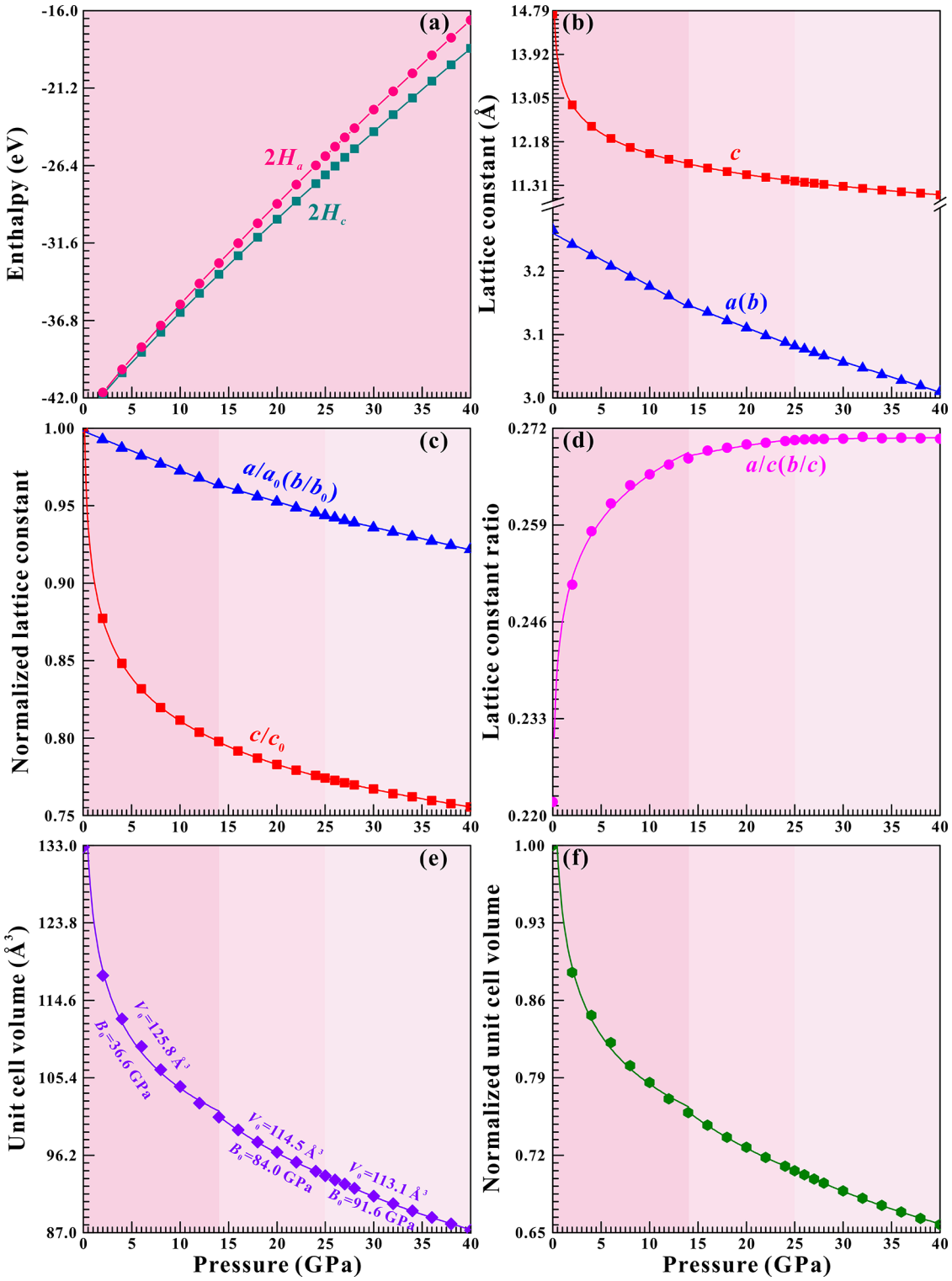

Figure 8. Theoretical calculation results on (a) enthalpy, (b) lattice constants, (c) normalized lattice constants, (d) lattice constant ratios, (e) unit cell volume, and (f) normalized unit cell volume as a function of pressure for WSSe over the pressure range of 0−40.0 GPa.

40.0 GPa, the *c* axis substantially shrunk by 24.4%, while the *a* and *b* axes only diminished by 7.8%. Therefore, the interlayer distance is of larger compressibility than the intralayer distance, which dovetails well with the highly anisotropic compression of 2D compounds.[1,15−20,26,59,60] Regarding the lattice constant ratio of a/c (b/c), it increased rapidly from 0.222 to 0.268 when the pressure was enhanced from 0 to 14.0 GPa, which evinces the dramatic decrease in interlayer distance. Noticeably, the a/c (b/c) ratio presented an almost plateau beyond 14.0 GPa, signaling the isotropic compressibility of *a* and *c* axes, which is caused by the substantial enhancement of interlayer repulsion forces as the adjacent layers get closer with applied pressure. In fact, the analogous phenomenon has also been observed in other characteristic TMDs (e.g., WSe_2, MoS_2, $MoSe_2$, $TiTe_2$, etc.).[1,17,61,62] Briefly, the *c* axis, c/c_0, a/c (b/c), W−W bond length, S−W−S bond angle, Se−W−Se bond

https://doi.org/10.1021/acs.inorgchem.3c02144
Inorg. Chem. 2023, 62, 16782−16793

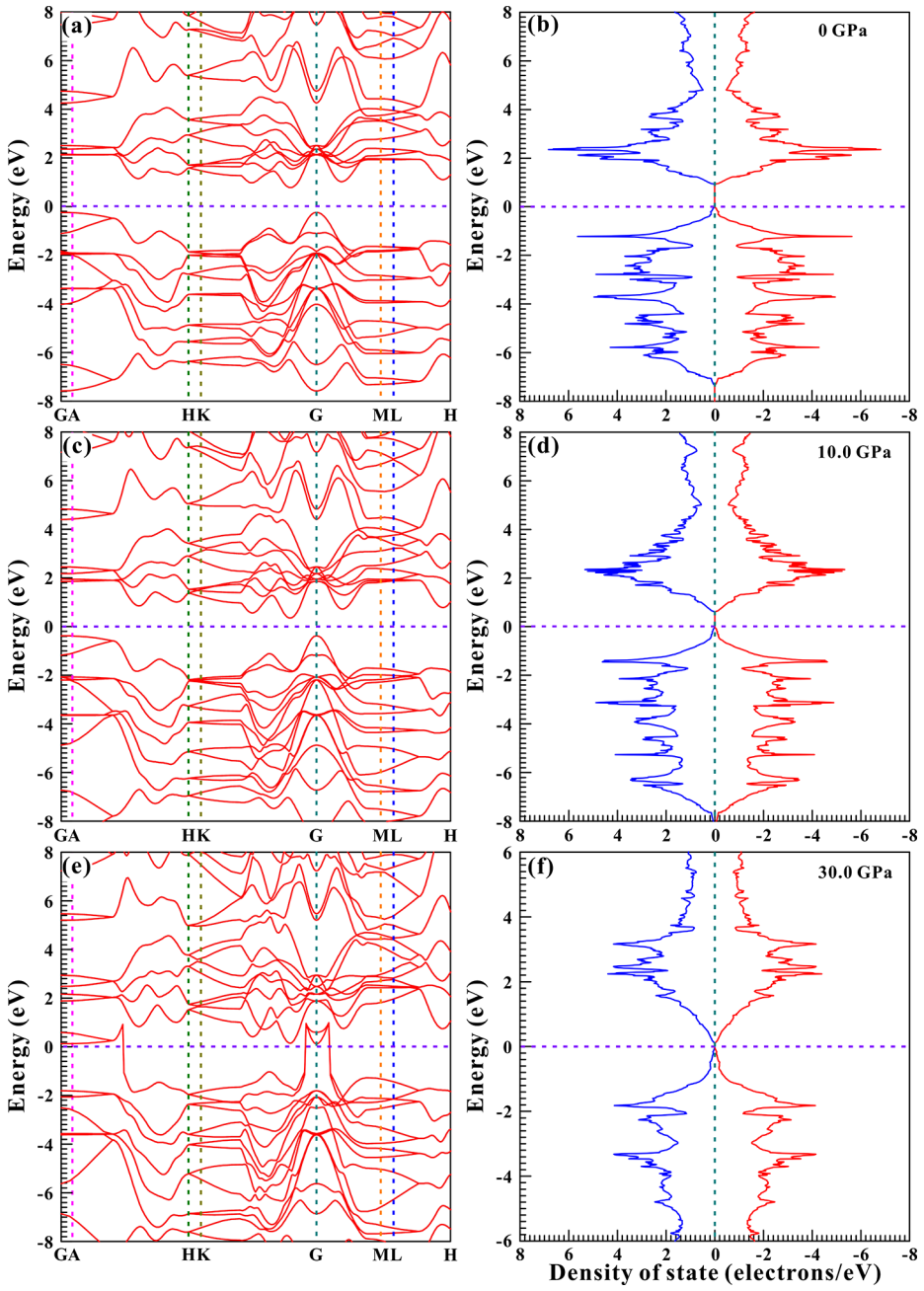

Figure 9. Electronic band structures (a, c, e) and correspondent density of states (b, d, f) for the $2H_c$ phase of WSSe at three representative pressures of 0, 10.0, and 30.0 GPa, respectively.

angle, and S−W−Se bond angle exhibited discernible inflection points at 14.0 GPa, accompanied by the faint discontinuity in unit cell volume, which offered explicit evidence for the occurrence of phase transition in WSSe at 14.0 GPa. In the meantime, the pressure-dependent unit cell volume data were fitted with the second-order Birch−Murnaghan equation of state (EOS), yielding the ambient bulk modulus (B_0) and ambient pressure volume (V_0) as 36.6 GPa and 125.8 Å^3 at 0−14.0 GPa, 84.0 GPa and 114.5 Å^3 at 14.0−25.0 GPa, and 91.6 GPa and 113.1 Å^3 at 25.0−40.0 GPa. The larger B_0 and smaller V_0 values manifested that the high-pressure phases of WSSe became denser and more incompressible.

To illuminate the source of metallization in WSSe, detailed analyses on the electronic band structures and their correspondent density of states (DOS) for the $2H_c$ and $2H_a$ phases of WSSe were carried out at 0−40.0 GPa. As depicted in Figure 9a, for the $2H_c$ phase of WSSe, it belongs to an indirect bandgap semiconductor with a finite bandgap energy of 1.02 eV under ambient conditions. Actually, our acquired bandgap energy of WSSe is smaller than the prior result.[11] Generally, DFT calculations underestimate the bandgap energy of TMDs, and further, the slight discrepancy in bandgap energy is tolerable.[26,63] With the rise in pressure, the conduction band minimum (CBM) progressively moved downward the Fermi level, causing the gradual narrowing of the bandgap. Thus, the bandgap energy reduced to 0.72 eV as the pressure was elevated to 10.0 GPa. Upon further pressurization to 30.0 GPa, the valence band maximum (VBM) crossed the Fermi level, hinting at the metallic

https://doi.org/10.1021/acs.inorgchem.3c02144
Inorg. Chem. 2023, 62, 16782−16793

character, which matches well with our high-pressure electrical conductivity results under nonhydrostatic conditions. As far as the $2H_a$ phase of WSSe, it possesses a similar bandgap energy of 1.02 eV under atmospheric conditions. As the pressure approached 40.0 GPa, a wide bandgap energy of 1.62 eV was acquired for the $2H_a$ phase, indicating the semiconducting property (see Figure S5 in the Supporting Information). Consequently, the electronic band structure results demonstrated that the metallization of WSSe possibly results from the bandgap overlap of the $2H_c$ phase under high pressure. In summary, the phase transition of WSSe occurred at 14.0 GPa and the metallic phase appeared beyond 30.0 GPa due to the bandgap closure, in good agreement with the high-pressure Raman scattering and electrical conductivity results under different hydrostatic environments.

4. CONCLUSIONS

In the present study, we have conducted a synthetic high-pressure investigation on the electrical transport properties and crystal structures for WSSe under different hydrostatic environments up to 40.0 GPa using a DAC in combination with Raman spectroscopy, electrical conductivity, HRTEM, and first-principles theoretical calculations. During the compressed process, WSSe took place in a phase transition at 15.2 GPa, followed by semiconductor-to-metal electronic switching at 25.3 GPa under nonhydrostatic conditions. Nevertheless, the phase transformation and electronic transition of WSSe were delayed by ∼2.0 GPa under hydrostatic conditions due to the faint deviatoric stress. Upon depressurization, the phase transition of WSSe showed good reversibility under different hydrostatic environments. These findings on WSSe extend our knowledge of the high-pressure crystalline structure evolution and electrical transport behaviors for the Janus TMD family and benefit the exploration of spintronics and optoelectrical devices.

■ ASSOCIATED CONTENT

Supporting Information

The Supporting Information is available free of charge at https://pubs.acs.org/doi/10.1021/acs.inorgchem.3c02144.

High-pressure Raman spectroscopy for WSSe under hydrostatic conditions and correspondent relationship between Raman shifts and pressure (Figure S1); temperature-dependent electrical conductivity results upon pressurization and depressurization (Figures S2 and S3); evolution of bond lengths and bond angles versus pressure (Figure S4); electronic band structures and their correspondent density of states for the $2H_a$ phase of WSSe at three characteristic pressures of 0, 20.0, and 40.0 GPa (Figure S5); detailed crystallographic data for WSSe under ambient conditions (Table S1); linear fitting results on the pressure-dependent Raman shifts and Raman fwhm's for WSSe under different hydrostatic environments (Tables S2 and S3); Raman peak intensity ratios upon pressurization and depressurization under different hydrostatic environments (Table S4); comparison of phase transition and metallization pressures of WSSe with the same periodic group of TMDs and Janus TMDs under different hydrostatic environments (Table S5) (PDF)

Accession Codes

CCDC 2289293−2289295 and 2294794 contain the supplementary crystallographic data for this paper. These data can be obtained free of charge via www.ccdc.cam.ac.uk/data_request/cif, or by emailing data_request@ccdc.cam.ac.uk, or by contacting The Cambridge Crystallographic Data Centre, 12 Union Road, Cambridge CB2 1EZ, UK; fax: +44 1223 336033.

■ AUTHOR INFORMATION

Corresponding Authors

Lidong Dai − *Key Laboratory of High-Temperature and High-Pressure Study of the Earth's Interior, Institute of Geochemistry, Chinese Academy of Sciences, Guizhou 550081, China;* orcid.org/0000-0002-9081-765X; Email: dailidong@vip.gyig.ac.cn

Haiying Hu − *Key Laboratory of High-Temperature and High-Pressure Study of the Earth's Interior, Institute of Geochemistry, Chinese Academy of Sciences, Guizhou 550081, China*; Email: huhaiying@vip.gyig.ac.cn

Authors

Meiling Hong − *Key Laboratory of High-Temperature and High-Pressure Study of the Earth's Interior, Institute of Geochemistry, Chinese Academy of Sciences, Guizhou 550081, China*

Xinyu Zhang − *Key Laboratory of High-Temperature and High-Pressure Study of the Earth's Interior, Institute of Geochemistry, Chinese Academy of Sciences, Guizhou 550081, China; University of Chinese Academy of Sciences, Beijing 100049, China*

Chuang Li − *Key Laboratory of High-Temperature and High-Pressure Study of the Earth's Interior, Institute of Geochemistry, Chinese Academy of Sciences, Guizhou 550081, China; University of Chinese Academy of Sciences, Beijing 100049, China*

Yu He − *Key Laboratory of High-Temperature and High-Pressure Study of the Earth's Interior, Institute of Geochemistry, Chinese Academy of Sciences, Guizhou 550081, China; University of Chinese Academy of Sciences, Beijing 100049, China;* orcid.org/0000-0001-6518-585X

Complete contact information is available at: https://pubs.acs.org/10.1021/acs.inorgchem.3c02144

Author Contributions

L.D. and H.H. conceived the idea and led the project. M.H., X.Z., and C.L. designed the experiments and conducted the X-ray diffraction, high-pressure Raman spectra, high-pressure electrical conductivity, and high-resolution transmission electron microscopy measurements. Y.H. carried out the first-principles theoretical calculations. L.D. and M.H. contributed to the analysis, interpretation, and discussion of results. M.H. wrote the manuscript with the help of all the authors. All the authors commented on the final manuscript. L.D. and H.H. supervised the project.

Notes

The authors declare no competing financial interest.

■ ACKNOWLEDGMENTS

We thank the editor of Professor Hiroshi Kageyama and three anonymous reviewers for their constructive and enlightened comments and suggestions in the reviewing process, which

helped us greatly in improving the manuscript. The authors acknowledge the technical support of the *in situ* high-pressure Raman scattering measurements provided by Professor Heping Li in the Key Laboratory of High-temperature and High-pressure Study of the Earth's Interior, Institute of Geochemistry, Chinese Academy of Sciences. This research was financially supported by the NSF of China (grant numbers 42072055, 42274137, and 42302047) and CAS Youth Interdisciplinary Team (grant number JCTD-2022-16). Numerical computations were performed at the Hefei Advanced Computing Center.

REFERENCES

(1) Wang, X.; Chen, X.; Zhou, Y.; Park, C.; An, C.; Zhou, Y.; Zhang, R.; Gu, C.; Yang, W.; Yang, Z. Pressure-induced iso-structural phase transition and metallization in WSe_2. *Sci. Rep.* **2017**, *7*, 46694 DOI: 10.1038/srep46694.

(2) Chen, K.; Tang, W.; Fu, M.; Li, X.; Ke, C.; Wu, Y.; Wu, Z.; Kang, J. Manipulation of the magnetic properties of Janus WSSe monolayer by the adsorption of transition metal atoms. *Nanoscale Res. Lett.* **2021**, *16*, 104 DOI: 10.1186/s11671-021-03560-9.

(3) Patel, S.; Dey, U.; Adhikari, N. P.; Taraphder, A. Electric field and strain-induced band-gap engineering and manipulation of the Rashba spin splitting in Janus van der Waals heterostructures. *Phys. Rev. B* **2022**, *106*, No. 035125.

(4) Petrić, M. M.; Kremser, M.; Barbone, M.; Qin, Y.; Sayyad, Y.; Shen, Y.; Tongay, S.; Finley, J. J.; Botello-Méndez, A. R.; Müller, K. Raman spectrum of Janus transition metal dichalcogenide monolayers WSSe and MoSSe. *Phys. Rev. B* **2021**, *103*, No. 035414.

(5) Karande, S. D.; Kaushik, N.; Narang, D. S.; Late, D.; Lodha, S. Thickness tunable transport in alloyed WSSe field effect transistors. *Appl. Phys. Lett.* **2016**, *109*, 142101 DOI: 10.1063/1.4964289.

(6) Guo, J.; Ke, C.; Wu, Y.; Kang, J. Strain engineering on the electronic and optical properties of WSSe bilayer. *Nanoscale Res. Lett.* **2020**, *15*, 97 DOI: 10.1186/s11671-020-03330-z.

(7) Verma, H.; Kale, A. J.; Prakash, C.; Harb, M.; Dixit, A. Enhanced photocatalytic activity in strain engineered Janus WSSe monolayers. *J. Electron. Mater.* **2021**, *50*, 7230−7239.

(8) Zhang, L.; Xia, Y.; Li, X.; Li, L.; Fu, X.; Cheng, J.; Pan, R. Janus two-dimensional transition metal dichalcogenides. *J. Appl. Phys.* **2022**, *131*, 230902 DOI: 10.1063/5.0095203.

(9) Chakraborty, S.; Raj, S. Anisotropic Rashba effect in two-dimensional non-Janus transition-metal dichalcogenide, *M*SSe (*M* = Mo, W) alloys. *Phys. Rev. B* **2023**, *107*, No. 035420.

(10) Kandemir, A.; Sahin, H. Bilayers of Janus WSSe: monitoring the stacking type via the vibrational spectrum. *Phys. Chem. Chem. Phys.* **2018**, *20*, 17380−17386.

(11) Zhou, W.; Chen, J.; Yang, Z.; Liu, J.; Ouyang, F. Geometry and electronic structure of monolayer, bilayer, and multilayer Janus WSSe. *Phys. Rev. B* **2019**, *99*, No. 075160.

(12) Yu, J.; Kuang, X.; Li, J.; Zhong, J.; Zeng, C.; Cao, L.; Liu, Z.; Zeng, Z.; Luo, Z.; He, T.; et al. Giant nonlinear optical activity in two-dimensional palladium diselenide. *Nat. Commun.* **2021**, *12*, 1083 DOI: 10.1038/s41467-021-21267-4.

(13) Di Bartolomeo, A.; Pelella, A.; Liu, X.; Miao, F.; Passacantando, M.; Giubileo, F.; Grillo, A.; Iemmo, L.; Urban, F.; Liang, S. Pressure-tunable ambipolar conduction and hysteresis in thin palladium diselenide field effect transistors. *Adv. Funct. Mater.* **2019**, *29*, 1902483 DOI: 10.1002/adfm.201902483.

(14) Tongay, S.; Zhou, J.; Ataca, C.; Lo, K.; Matthews, T. S.; Li, J. B.; Grossman, J. C.; Wu, J. Thermally driven crossover from indirect toward direct bandgap in 2D semiconductors: $MoSe_2$ versus MoS_2. *Nano Lett.* **2012**, *12*, 5576−5580.

(15) Chi, Z. H.; Zhao, X. M.; Zhang, H.; Goncharov, A. F.; Lobanov, S. S.; Kagayama, T.; Sakata, M.; Chen, X. J. Pressure-induced metallization of molybdenum disulfide. *Phys. Rev. Lett.* **2014**, *113*, No. 036802.

(16) Nayak, A. P.; Bhattacharyya, S.; Zhu, J.; Liu, J.; Wu, X.; Pandey, T.; Jin, C.; Singh, A. K.; Akinwande, D.; Lin, J. F. Pressure-induced semiconducting to metallic transition in multilayered molybdenum disulphide. *Nat. Commun.* **2014**, *5*, 3731.

(17) Zhao, Z.; Zhang, H.; Yuan, H.; Wang, S.; Lin, Y.; Zeng, Q.; Xu, G.; Liu, Z.; Solanki, G. K.; Patel, K. D.; Cui, Y.; Hwang, H. Y.; Mao, W. L. Pressure induced metallization with absence of structural transition in layered molybdenum diselenide. *Nat. Commun.* **2015**, *6*, 7312.

(18) Duwal, S.; Yoo, C. S. Shear-induced isostructural phase transition and metallization of layered tungsten disulfide under nonhydrostatic compression. *J. Phys. Chem. C* **2016**, *120*, 5101−5107.

(19) Saha, P.; Ghosh, B.; Jana, R.; Mukherjee, G. D. Structural anomalies in exfoliated WS_2: High pressure investigations on monolayer and nanocrystalline tungsten disulfide. *J. Appl. Phys.* **2018**, *123*, 204306 DOI: 10.1063/1.5027020.

(20) Shen, P.; Ma, X.; Guan, Z.; Li, Q.; Zhang, H.; Liu, R.; Liu, B.; Yang, X.; Dong, Q.; Cui, T.; et al. Linear tunability of the band gap and two-dimensional (2D) to three-dimensional (3D) isostructural transition in WSe_2 under high pressure. *J. Phys. Chem. C* **2017**, *121*, 26019−26026.

(21) Zhuang, Y.; Dai, L.; Wu, L.; Li, H.; Hu, H.; Liu, K.; Yang, L.; Pu, C. Pressure-induced permanent metallization with reversible structural transition in molybdenum disulfide. *Appl. Phys. Lett.* **2017**, *110*, 122103 DOI: 10.1063/1.4979143.

(22) Zhuang, Y.; Dai, L.; Li, H.; Hu, H.; Liu, K.; Yang, L.; Pu, C.; Hong, M.; Liu, P. Deviatoric stresses promoted metallization in rhenium disulfide. *J. Phys. D: Appl. Phys.* **2018**, *51*, 165101.

(23) Yang, L.; Dai, L.; Li, H.; Hu, H.; Liu, K.; Pu, C.; Hong, M.; Liu, P. Pressure-induced metallization in $MoSe_2$ under different pressure conditions. *RSC Adv.* **2019**, *9*, 5794−5803.

(24) Yang, L.; Dai, L.; Li, H.; Hu, H.; Liu, K.; Pu, C.; Hong, M.; Liu, P. Characterization of the pressure-induced phase transition of metallization for $MoTe_2$ under hydrostatic and non-hydrostatic conditions. *AIP Adv.* **2019**, *9*, No. 065104, DOI: 10.1063/1.5097428.

(25) Xia, J.; Li, D. F.; Zhou, J. D.; Yu, P.; Lin, J. H.; Kuo, J. L.; Li, H. B.; Liu, Z.; Yan, J. X.; Shen, Z. X. Pressure-induced phase transition in Weyl semimetallic WTe_2. *Small* **2017**, *13*, 1701887 DOI: 10.1002/smll.201701887.

(26) Hong, M. L.; Dai, L. D.; Hu, H. Y.; Zhang, X. Y.; Li, C.; He, Y. High-pressure structural phase transitions and metallization in layered HfS_2 under different hydrostatic environments up to 42.1 GPa. *J. Mater. Chem. C* **2022**, *10*, 10541−10550.

(27) Bera, A.; Singh, A.; Sorb, Y. A.; Jenjeti, R. N.; Muthu, D. V. S.; Sampath, S.; Narayana, C.; Waghmare, U. V.; Sood, A. K. Chemical ordering and pressure-induced isostructural and electronic transitions in MoSSe crystal. *Phys. Rev. B* **2020**, *102*, No. 014103.

(28) Zhang, D. J.; Chen, X. Y.; Jiang, P.; Li, Y. G.; Zheng, X. H.; Liu, Z.; Miao, M. S.; Huang, H. M.; Li, Y. L. Pressure-tuned one- to quasi-two-dimensional structural phase transition and superconductivity in LiP15. *Phys. Rev. B* **2022**, *105*, No. 094109.

(29) Li, Y. G.; Li, Y. L.; Sa, B. S.; Ahuja, R. Review of two-dimensional materials for photocatalytic water splitting from a theoretical perspective. *Catal. Sci. Technol.* **2017**, *7*, 545−559.

(30) Klotz, S.; Chervin, J. C.; Munsch, P.; Le Marchand, G. Hydrostatic limits of 11 pressure transmitting media. *J. Phys. D: Appl. Phys.* **2009**, *42*, No. 075413.

(31) Celeste, A.; Borondics, F.; Capitani, F. Hydrostaticity of pressure-transmitting media for high pressure infrared spectroscopy. *High Press. Res.* **2019**, *39*, 608−618.

(32) Takemura, K. Hydrostaticity in high pressure experiments: some general observations and guidelines for high pressure experimenters. *High Press. Res.* **2021**, *41*, 155−174.

(33) Wang, P.; Wang, Y. G.; Qu, J. Y.; Zhu, Q.; Yang, W. G.; Zhu, J. L.; Wang, L. P.; Zhang, W. W.; He, D. W.; Zhao, Y. S. Pressure-induced structural and electronic transitions, metallization, and enhanced visible-light responsiveness in layered rhenium disulphide. *Phys. Rev. B* **2018**, *97*, No. 235202.

(34) Trivedi, D. B.; Turgut, G.; Qin, Y.; Sayyad, M. Y.; Hajra, D.; Howell, M.; Liu, L.; Yang, S. J.; Patoary, N. H.; Li, H.; et al. Room-temperature synthesis of 2D Janus crystals and their heterostructures. *Adv. Mater.* **2020**, *32*, 2006320.
(35) Zheng, B. Y.; Ma, C.; Li, D.; Lan, J. Y.; Zhang, Z.; Sun, X. X.; Zheng, W. H.; Yang, T. F.; Zhu, C. G.; Ouyang, G.; et al. Band alignment engineering in two-dimensional lateral heterostructures. *J. Am. Chem. Soc.* **2018**, *140*, 11193−11197.
(36) Zheng, B. Y.; Li, D.; Zhu, C. G.; Lan, J. Y.; Sun, X. X.; Zheng, W. H.; Liu, H. W.; Zhang, X. H.; Zhu, X. L.; Feng, Y. X.; et al. Dual-channel type tunable field-effect transistors based on vertical bilayer $WS_{2(1-x)}Se_{2x}/SnS_2$ heterostructures. *Infomat* **2020**, *2*, 752−760.
(37) Larson, A. C.; Von Dreele, R. B. General structure analysis system (GSAS). *Los Alamos National Laboratory Report LAUR* **2005**, 86−748.
(38) Kim, J. H.; Yun, J. H.; Song, Y. J.; Rhyee, J. S. Anisotropic thermoelectric and superconducting properties of the bulk misfit-layered $(SnSe)_{1.17}(TaSe_2)$ compound. *Curr. Appl. Phys.* **2021**, *28*, 1−6.
(39) Mohammed, H. G.; Albarody, T. M. B.; Al-Jothery, H. K. M.; Mustapha, M.; Sultan, N. M. A study of crystalline-texture and anisotropic properties of hexagonal $BaFe_{12}O_{19}$ sintered by in-situ magnetic-anisotropy spark plasma sintering (MASPS). *J. Magn. Magn. Mater.* **2022**, *553*, 169268.
(40) Edmond, J. M.; Paterson, M. S. Strength of solid pressure media and implications for high pressure apparatus. *Contrib. Mineral. Petrol.* **1971**, *30*, 141−160.
(41) Hong, M. L.; Dai, L. D.; Hu, H. Y.; Zhang, X. Y.; Li, C.; He, Y. Pressure-induced structural phase transition and metallization of $CrCl_3$ under different hydrostatic environments up to 50.0 GPa. *Inorg. Chem.* **2022**, *61*, 4852−4864.
(42) Dai, L. D.; Liu, K. X.; Li, H. P.; Wu, L.; Hu, H. Y.; Zhuang, Y. K.; Yang, L. F.; Pu, C.; Liu, P. F. Pressure-induced irreversible metallization accompanying the phase transitions in Sb_2S_3. *Phys. Rev. B* **2018**, *97*, No. 024103.
(43) Kresse, G.; Furthmüller, J. Efficient iterative schemes for *ab initio* total-energy calculations using a plane-wave basis set. *Phys. Rev. B* **1996**, *54*, 11169−11186.
(44) Kresse, G.; Furthmüller, J. Efficiency of ab-initio total energy calculations for metals and semiconductors using a plane-wave basis set. *Comput. Mater. Sci.* **1996**, *6*, 15−50.
(45) He, Y.; Sun, S. C.; Kim, D. Y.; Jang, B. G.; Li, H. P.; Mao, H.-K. Superionic iron alloys and their seismic velocities in Earth's inner core. *Nature* **2022**, *602*, 258−262.
(46) Sun, S. C.; He, Y.; Yang, J. Y.; Lin, Y. F.; Li, J. F.; Kim, D. Y.; Li, H. P.; Mao, H.-K. Superionic effect and anisotropic texture in Earth's inner core driven by geomagnetic field. *Nat. Commun.* **2023**, *14*, 1656.
(47) Blöchl, P. E.; Jepsen, O.; Andersen, O. K. Improved tetrahedron method for Brillouin-zone integrations. *Phys. Rev. B: Condens. Matter Mater. Phys.* **1994**, *49*, 16223−16233.
(48) Perdew, J. P.; Burke, K.; Ernzerhof, M. Generalized gradient approximation made simple. *Phys. Rev. Lett.* **1996**, *77*, 3865−3868.
(49) Grimme, S.; Antony, J.; Ehrlich, S.; Krieg, H. A consistent and accurate *ab initio* parametrization of density functional dispersion correction (DFT-D) for the 94 elements H-Pu. *J. Chem. Phys.* **2010**, *132*, 154104.
(50) Duan, X. D.; Wang, C.; Fan, Z.; Hao, G. L.; Kou, L. Z.; Halim, U.; Li, H. L.; Wu, X. P.; Wang, Y. C.; Jiang, J. H.; et al. Synthesis of $WS_{2x}Se_{2-2x}$ alloy nanosheets with composition-tunable electronic properties. *Nano Lett.* **2016**, *16*, 264−269.
(51) Sivakumar, A.; Dhas, S. S. J.; Dai, L. D.; Mowlika, V.; Sivaprakash, P.; Kumar, R. S.; Almansour, A. I.; Arumugam, S.; Kim, I.; Dhas, S. A. M. B. X-ray diffraction and optical spectroscopic analysis on the crystallographic phase stability of shock wave loaded L-Valine. *J. Mater. Sci.* **2023**, *58*, 9210−9220.
(52) Kubra, K.; Islam, M. R.; Khan, M. S. H.; Islam, M. S.; Hasan, M. T. Study of two-dimensional Janus WXY (X≠Y= S, Se, and Te) trilayer homostructures for photovoltaic applications using DFT screening of different stacking patterns. *ACS Omega* **2022**, *7*, 12947−12955, DOI: 10.1021/acsomega.2c00244.
(53) Gong, Y. B.; Zhou, Q.; Liu, Y.; Fu, X. P.; Yao, M. G.; Huang, X. L.; Huang, Y. P.; Gao, H. X.; Li, F. F.; Cui, T. Increasing interlayer coupling prevented the deformation in compressed multilayer WSe_2. *J. Phys. Chem. C* **2018**, *122*, 10261−10266.
(54) Hong, M. L.; Dai, L. D.; Hu, H. Y.; Zhang, X. Y.; Li, C.; He, Y. Pressure-driven structural phase transitions and metallization in the two-dimensional ferromagnetic semiconductor $CrBr_3$. *Dalton Trans.* **2023**, *52*, 7290−7301.
(55) Zhang, W. X.; Yin, Y.; He, C. Lowering the Schottky barrier height of G/WSSe van der Waals heterostructures by changing the interlayer coupling and applying external biaxial strain. *Phys. Chem. Chem. Phys.* **2020**, *22*, 26231−26240.
(56) Ju, L.; Bie, M.; Tang, X.; Shang, J.; Kou, L. Z. Janus WSSe monolayer: An excellent photocatalyst for overall water splitting. *ACS Appl. Mater. Interfaces* **2020**, *12*, 29335−29343, DOI: 10.1021/acsami.0c06149.
(57) Naumov, P. G.; ElGhazali, M. A.; Mirhosseini, H.; Sü*β*, V.; Morosan, E.; Felser, C.; Medvedev, S. A. Pressure-induced metallization in layered $ReSe_2$. *J. Phys.: Condens. Matter* **2018**, *30*, No. 035401.
(58) Xiao, F.; Lei, W.; Wang, W.; Autieri, C.; Zheng, X. J.; Ming, X.; Luo, J. L. Pressure-induced structural transition, metallization, and topological superconductivity in PdSSe. *Phys. Rev. B* **2022**, *105*, No. 115110.
(59) Zhou, Y.; Zhang, B.; Chen, X.; Gu, C.; An, C.; Zhou, Y.; Cai, K.; Yuan, Y.; Chen, C.; Wu, H.; et al. Pressure-induced metallization and robust superconductivity in pristine 1*T*-$SnSe_2$. *Adv. Electron. Mater.* **2018**, *4*, 1800155 DOI: 10.1002/aelm.201800155.
(60) Shi, Y.; Song, H.; Li, N.; Wu, X.; Wang, K.; Wu, Y.; Ye, G.; Huang, H. High-pressure structural stability and bandgap engineering of layered tin disulfide. *Appl. Phys. Lett.* **2022**, *121*, 114101 DOI: 10.1063/5.0107303.
(61) Goncharov, A. F.; Bykov, M.; Bykova, E.; Glazyrin, K.; Prakapenka, V.; Cao, Z. Y.; Chen, X. J. Structure and stability of 2H_a-MoS_2 at high pressure and low temperatures. *Phys. Rev. B* **2020**, *102*, No. 064105.
(62) Rajaji, V.; Dutta, U.; Sreeparvathy, P. C.; Sarma, S. C.; Sorb, Y. A.; Joseph, B.; Sahoo, S.; Peter, S. C.; Kanchana, V.; Narayana, C. Structural, vibrational, and electrical properties of 1*T*-$TiTe_2$ under hydrostatic pressure: Experiments and theory. *Phys. Rev. B* **2018**, *97*, No. 085107.
(63) Ruiz-Fuertes, J.; López-Moreno, S.; López-Solano, J.; Errandonea, D.; Segura, A.; Lacomba-Perales, R.; Muñoz, A.; Radescu, S.; Rodríguez-Hernández, P.; Gospodinov, M.; et al. Pressure effects on the electronic and optical properties of AWO_4 wolframites (*A* = Cd, Mg, Mn, and Zn): The distinctive behavior of multiferroic $MnWO_4$. *Phys. Rev. B* **2012**, *86*, No. 125202.